

Large Eddy Simulation of Rotating Turbulent Convection Using the Estimation Subgrid Scale Model

S. Kimmel⁽¹⁾, F.P. Deek⁽²⁾

⁽¹⁾ Visiting Research Scientist
Information Technology Program

New Jersey Institute of Technology, Newark, NJ 07102

⁽²⁾ College of Science and Liberal Arts

New Jersey Institute of Technology, Newark, NJ 07102

CAMS Report 0304-34, Spring 2004

Center for Applied Mathematics and Statistics

NJIT

Equation Chapter 1 Section 1
LES of Rotating Finite Source Convection

Shari J. Kimmel-Klotzkin
Visiting Research Scientist
New Jersey Institute of Technology
Information Technology Program
323 M.L.King Blvd.
University Heights Newark, NJ 07102-1982, USA
E-mail: sklotzkin@alumni.rutgers.edu
Phone: 973.596.3676
Fax: 973.565.0586

Fadi P. Deek
Acting Dean, College of Science and Liberal Arts
New Jersey Institute of Technology
College of Science and Liberal Arts
323 M.L.King Blvd.
University Heights Newark, NJ 07102-1982, USA
E-mail: Fadi.Deek@njit.edu
Phone: 973.596.3676
Fax: 973.565.0586

Abstract

Numerical simulations of turbulent convection under the influence of rotation will help to study mixing in oceanic flows. In this study, a large eddy simulation (LES) with the Smagorinsky subgrid scale model is used to compute the time evolution of a rotating convection flow generated by a buoyancy source of finite size at a relatively high Rayleigh number. The computed velocity and temperatures are in better agreement with a direct numerical simulation (DNS) than LES simulations with constant eddy viscosity.

These results also demonstrate that the qualitative behavior of vortices which form under the source depend on the aspect ratio of the flow. For source diameters that are small compared to the size of the domain, the vortices propagate away from the source. On the other hand, if the ratio of source diameter to domain size is relatively large, the vortices remain under the source. Evidence from other studies suggests that a rim current around the edge of the source develops for intermediate values of this aspect ratio.

Though the results are qualitatively similar to a direct numerical simulation (DNS) and other LES, in this simulation the flow remains laminar much longer than the DNS predicts. This particular flow is complicated by the turbulence transition between the convective plume and the quiescent ambient fluid, and an eddy viscosity model is inadequate to accurately model this type of flow. In addition, the Smagorinsky model is not consistent in a noninertial reference frame. A more accurate simulation of rotating convection requires an alternate subgrid scale model. In particular, the estimation model has demonstrated better results for other types of rotating flows and is the recommended subgrid scale model for future work.

Nomenclature

All quantities have been nondimensionalized by length scale H (depth of the computational domain) and the velocity scale κ / H .

B_o	Buoyancy flux
B_{oavg}	Average buoyancy flux over the circular source
B_{omax}	Maximum buoyancy flux in the circular source
c_p	Specific gravity
C_S	Smagorinsky model constant
D	Diameter of finite buoyancy source
f	Period of rotation
$f(x)$	Unfiltered function
$\bar{f}(x)$	Filtered function (resolved on LES grid)
F_T	Buoyancy forcing term
g	Acceleration due to gravity
$G(x)$	Filter function
g'	Reduced gravity
H	Depth of computational domain
h_s	Depth to which buoyancy flux is applied
L_x, L_y	Horizontal size of computational domain
P	Pressure
Pr	Prandtl number
Pr_T	Turbulent Prandtl number
r	Radial coordinate direction
Ra_f	Rayleigh number defined base on buoyancy flux
Ro^*	Natural Rossby number
r_{unif}	Radius of uniform region in the buoyancy source
S_{ij}	Rate of strain tensor
T	Temperature
Ta	Taylor number
u_H	Horizontally averaged velocity
u_i	Component of velocity
u_i	Velocity component
x, y, z	Coordinate directions in physical space
α	Volumetric thermal expansion coefficient
δ_{ij}	Kronecker delta
Δ	Factor in Smagorinsky model which depends on the mesh size
$\Delta x, \Delta y, \Delta z$	Grid cell sizes in the x, y and z directions
Θ	Period of rotation
κ	Thermal diffusivity

ν	Molecular diffusivity
ν_h	Constant eddy viscosity in the horizontal direction (used in [5])
ν_T	Eddy viscosity for present study
ν_v	Constant eddy viscosity in the vertical direction (used in [5])
ρ_0	Density of ambient fluid
ρ	Local fluid density
Ω	Rotation rate of frame of reference

1. Introduction

Ocean circulations are key to understanding global climate changes. Major climatic changes, such as an ice age, are thought to be accompanied by significant changes in ocean circulations. Since the average temperature of the ocean is about 1 degree Celsius, it acts as a huge heat sink that can mitigate the effects of global warming. In fact, the lower atmosphere receives almost as much heat from the ocean as from the sun in arctic regions. Convection or similar buoyancy force is the driving force for some large scale oceanic circulations, including thermohaline circulations. Natural phenomena that cause buoyancy driven circulations in the ocean include evaporation, extreme weather conditions such as storms, freezing at the surface, and heating through the ocean floor causing a megaplume event. The process of freezing the surface water causes a buoyancy driven flow due to increased salinity just below the ice because the colder water cannot hold as much dissolved salt.

Some of the current research in environmental turbulent convection focuses on deep water formation, which is thought to be related to major climatic events. Deep water is very cold, fairly dense water, generally found in arctic regions. New deep water formed near the surface tends to sink by creating a chimney, which consists of a relatively homogeneous water column surrounded by more stratified waters. Only extreme conditions can cause sinking all the way to the ocean floor. Though such conditions are not common, they are most often found in the Greenland and Weddell Seas [1]. Initially, cooling simply deepens the mixed layer near the surface. When the mixed layer reaches a certain depth, a thermobaric instability occurs and the chimneys form.

Global oceanic (and atmospheric) circulation simulations do not provide adequate long-term predictions [2] of the flow field. Using field studies and experiments to clarify the important physical processes will assist in the development of better numerical models. Localized simulations have had more success, such as a numerical model of turbulent line buoyant plumes which occur due to brine rejection when cracks in ice refreeze [3].

A direct numerical simulation (DNS) for an unstratified ambient fluid has been performed successfully [4]. A Rayleigh number bordering on the turbulent regime requires hundreds of hours of CPU time and 16 million grid points. DNS techniques give an “exact” solution to the governing equation but are limited to relatively low Reynolds number due to insufficient computational resources. By using a large eddy simulation (LES), which involves modeling the small scales and resolving only the large scales, a computation could be performed at a higher Rayleigh number using a half a million grid points and less than 100 hours of CPU time. The current study involves using an LES to simulate rotating turbulent convection with a finite source. Detailed quantitative comparisons between these computations and the DNS of [4]

and the LES of [5] would validate the use of the Smagorinsky model for this type of flow.

2. Background

For large scale geophysical flows, the Coriolis effect due to the rotation of the earth becomes an important influence in the evolution of the flow. When significant rotation is added to turbulent Rayleigh-Bérnard convection, the cells orient radially as a result of the radial acceleration which increases with increasing radius. Higher rotation rates breaks up these rolls and very high rotation induces the formation of cyclonic and anticyclonic vortices. The structure of high Rayleigh number turbulent convective flows under the influence of rotation has been previously investigated experimentally by Rossby [6], Boubnov and Golitsyn [7] Fernando, *et al.* [8], Brickman and Kelly [9] and Maxworthy and Narimousa [10]. Field studies in arctic regions [11,12] examine the chimney structure and corroborate well with experimental results. Because of the very large scale of oceanic flows, simulation of a realistic geophysical flow field is still beyond the capabilities of current computational resources. However, recent smaller scale simulations have been able to obtain flow fields that agree well with experimental studies, including the DNS of Chan [4] and LES of Jones and Marshall [5], Lavelle and Baker [3], Julien, *et al.* [13], and Cui and Street [14].

The dimensionless parameters that define this type of flow are the Rayleigh number, the Prandtl number and the Taylor number. The Rayleigh number, which represents the ratio of buoyancy forces to viscous forces, can be expressed in terms of the surface buoyancy flux:

$$Ra_f = \frac{B_o H^4}{\kappa^2 \nu} \quad (1)$$

where

$$B_o = \frac{\alpha g \kappa \frac{\partial T}{\partial z}}{\rho_o c_p} \quad (2)$$

which is the buoyancy flux of the fluid resulting from an imposed temperature gradient at the at the boundary. The Taylor number, which represents the ratio of rotational forces to viscous forces, and the Prandtl number, which gives the relative importance of the momentum diffusivity to the thermal diffusivity, are expressed as follows:

$$Ta = \frac{4\Omega^2 H^4}{\nu^2} \quad (3)$$

and

$$Pr = \nu / \kappa \quad (4)$$

The previous parameters are based on molecular quantities. However, this flow may be better described using parameters that do not depend on molecular quantities. For instance, a natural Rossby number is defined as

$$Ro^* = \frac{B_o^{1/2}}{f^{3/2} H} = Ra_f^{1/2} Pr^{-1} Ta^{-3/4} \quad (5)$$

which is less than one when rotational effects are significant.

3. Numerical Methodology

The governing equations are the incompressible Navier-Stokes equations with the Boussinesq approximation plus the energy equation. The LES equations are obtained by applying spatial filtering to the governing equations. The spatial filtering is defined by the integral relation

$$\bar{f}(x) = \int f(x') G(x) dx' \quad (6)$$

where $G(x)$ is the Fourier cutoff filter and the overbar (\bar{f}) represents a filtered quantity. The filtered equations are

$$\frac{\partial \bar{u}_j}{\partial x_j} = 0 \quad (7)$$

$$\frac{\partial \bar{u}_i}{\partial t} + \frac{\partial \bar{u}_i \bar{u}_j}{\partial x_j} + \sqrt{Ta} Pr \bar{u}_j \varepsilon_{ij3} = -\frac{\partial P}{\partial x_i} + Pr \frac{\partial^2 \bar{u}_i}{\partial x_j \partial x_j} - \frac{\partial}{\partial x_j} \tau_{ij} + Pr Ra_f \bar{T} \delta_{i3} \quad (8)$$

$$\frac{\partial \bar{T}}{\partial t} + \frac{\partial \bar{u}_j \bar{T}}{\partial x_j} = \frac{\partial^2 \bar{T}}{\partial x_j \partial x_j} + \frac{\partial}{\partial x_j} \tau_{\theta j} + F_T \quad (9)$$

where F_T is a nondimensional forcing term that is used to apply a buoyancy. The above equations are nondimensionalized using the diffusivity κ and the layer width H .

The effects of the turbulent scales, or unresolved subgrid scales (SGS), removed by the filtering operation on the filtered (resolved) scales is accounted for by the following subgrid scale quantities

$$\tau_{ij} = \overline{u_i u_j} - \bar{u}_i \bar{u}_j \quad (10)$$

$$\tau_{\theta j} = \overline{u_j T} - \bar{u}_j \bar{T} \quad (11)$$

These SGS stresses are modeled in terms of the resolved quantities. The Smagorinsky model, which uses an eddy viscosity formulation, is the most common SGS model. The subgrid scale stresses are defined as

$$\tau_{ij} = -2\nu_T \bar{S}_{ij} + \frac{1}{3} \tau_{kk} \delta_{ij} \quad (12)$$

$$\tau_{\theta j} = \frac{\nu_T}{Pr_T} \frac{\partial \bar{T}}{\partial x_j} \quad (13)$$

where $Pr_T=1$ and the resolved rate of strain tensor, \bar{S}_{ij} , is defined as

$$S_{ij} = \frac{1}{2} \left(\frac{\partial \bar{u}_i}{\partial x_j} + \frac{\partial \bar{u}_j}{\partial x_i} \right) \quad (14)$$

For the Smagorinsky model, the eddy viscosity is defined as

$$\nu_T = \begin{cases} (C_s \Delta)^2 \left(2\bar{S}_{ij}^2 - \frac{Ra_f}{Pr Pr_T} \frac{\partial \bar{T}}{\partial x_i} \delta_{i3} \right)^{1/2} & \text{if } \left(2\bar{S}_{ij}^2 - \frac{Ra_f}{Pr Pr_T} \frac{\partial \bar{T}}{\partial x_i} \delta_{i3} \right) > 0 \\ 0 & \text{otherwise} \end{cases} \quad (15)$$

which includes a term to take into account mixing due to statically unstable conditions [15]. Several attempts at calculating an optimal value for C_s using theoretical methods [16,17] have produced values between 0.1 and 0.2. The present study uses $C_s=0.21$ which is a typical value for turbulent convection [18]. The turbulent Prandlt number $Pr_T \equiv \frac{\kappa_T}{\nu_T} = 1$, and Δ , a length scale determined by the mesh size, is usually defined as

$$\Delta = (\Delta x \Delta y \Delta z)^{1/3} \quad (16)$$

For wall bounded flows, the maximum Δz is often an order of magnitude greater than the minimum value due to the finer grid spacing near the wall. An alternative definition for Δ which would keep it constant throughout the domain is

$$\Delta = \Delta x = \Delta y \quad (17)$$

These equations are solved numerically using a pseudo-spectral code developed by Chan [4]. The grid points in the z -direction are more finely spaced near the boundaries using Legendre-Gauss-Lobatto collocation points. Temporal advancement is accomplished using the Crank-Nicolson scheme for the viscous terms and the Adams-Bashforth method for the subgrid scale stresses. The Smagorinsky model was implemented exactly as in [18].

4. Description of Flow

The current work uses the LES method to study thermal plumes and chimneys in a rotating reference frame. The three dimensional rectangular domain with periodic boundary conditions in the horizontal directions and a no-slip, insulated bottom boundary is shown in figure 1. The depth of the domain, H , is defined to be 1, so the

horizontal dimensions, L_x and L_y , define the aspect ratio of the domain. The top surface boundary conditions are stress-free for the velocity and a circular heat source of radius R centered on the surface for the temperature. The magnitude of the circular finite source varies from a maximum in the center to zero at the edge, and the rest of the boundary is insulated.

The buoyancy force on the surface can be treated either as a boundary condition or as a forcing function in the simulation distributed over a finite depth, h_s [5]. The latter method is used in this study because it gives better results for this type of flow [19]. The heat flux source is implemented by setting

$$F_T = \begin{cases} -2 \frac{1-(1-z)/h_s}{h_s} \frac{B_o}{\alpha g} & r < r_{unif} \\ -\frac{1-(1-z)/h_s}{h_s} \frac{B_o}{\alpha g} \left\{ 1.0 + \cos \left[\frac{\pi(r-r_{unif})}{D-r_{unif}} \right] \right\} & r < D \text{ and } z \leq h_s \\ 0 & r > D \text{ or } z > h_s \end{cases} \quad (18)$$

in equation (9). The forcing is applied over top 6% of the domain and is scaled so that it would be equivalent to a concentrated heat flux of B_o applied on the upper surface as a boundary condition.

The development of a flow field due to a finite circular cooling source at the surface in the presence of rotation occurs in three stages. Initially, the flow is laminar natural convection. If the Rayleigh number is high enough, individual plumes start to develop from the mixed layer signifying the onset of turbulence. The flow behavior is convection dominated until the mixed layer reaches a critical depth. Then the rotation starts limiting the horizontal spreading of the plumes. Eventually the flow becomes quasi two-dimensional and geostrophic in which the pressure forces balance the Coriolis force. For higher rotation rates and larger Rayleigh numbers, the flow becomes more three-dimensional and less geostrophic.

5. Results

Results for a convection-dominated case [19] were promising when compared with DNS results (Chan, 1996) for $Ra_f=10^7$ and $Ta=10^6$. LES of a rotating finite source were computed with $Ra_f=5 \times 10^{10}$ and $Ta=3 \times 10^8$ for a large D/L_x of $1/2$ and a small D/L_x of $1/5$. Since the purpose of LES is to attempt to simulate more realistic flows, a relatively high Rayleigh number was chosen. However, the natural Rossby number [10], which is most representative of the type of flow (flow regime), and the aspect ratio were chosen to enable comparison with the LES of Jones and Marshall [5], hereafter referred to as JM, and with the DNS of Chan [4]. The Rossby number

represent the ratio of inertial to rotational effects, and the natural Rossby number is defined based on rotationally effected scales as follows:

$$Ro^* = \frac{B_o^{1/2}}{f^{3/2}H} = Ra_f^{1/2} Pr^{-1} Ta^{3/4} \quad (19)$$

$Ro^*=0.1$ for most of these simulations, which puts the flow in the transitional regime. The LES was initialized with zero temperature and velocity fields. A distributed source boundary condition and a free surface are applied at the upper surface, with an insulated no-slip bottom boundary, similar to the boundary conditions used by JM. All quantities are nondimensionalized by a characteristic length scale, H , temperature scale, $\frac{B_o H}{\alpha g \kappa}$, and velocity scale $\frac{\kappa}{H}$.

5.1 Large D/L_x Case

The sensitivity of the computation to the grid spacing, eddy viscosity model and surface heat flux was studied, and these results were compared with the results of JM. JM performed an LES using finite differencing spacial discretization with a constant eddy viscosity which is 25 times larger in the horizontal direction than in the vertical. The parameters for the simulations of the current study as well as those from the relevent JM cases are shown in Table I. Horizontally averaged velocity,

$u_H = \frac{\overline{u^2 + v^2}}{(B_o H)^{1/3}}$, and reduced gravity, g' , vertical profiles are presented for all cases

after two rotation periods. In the following discussion, unless otherwise specified, $Ro^* = 0.1$.

As shown by temperature contours in a vertical slice through the center of the domain in figure 2, the plumes take about $1\frac{1}{2}$ rotations to reach the bottom boundary. This is slower than in the results of JM in which it takes less than one rotation. Within the first rotation the vortices in JM are well developed, but in this study, they are barely starting to appear after $1\frac{1}{2}$ rotations. Perhaps this discrepancy is a result of one of the drawbacks of the Smagorinsky model. Intuitively, the plumes should develop most quickly in a region of maximum surface heat flux, but the eddy viscosity in this simulation is the largest where the velocity gradients are most significant. Also, since JM uses finite differencing, the artificial viscosity may play a more important role than in the current study. Though asymmetry is an important property of turbulent flows, it is not apparent during the time period of this simulation for both the vertical contours and horizontal contours (figures 2 and 3). In spite of the discrepancies in the instantaneous results, some qualitative similarities are apparent in horizontally averaged quantities. The major differences between the current study and JM are the magnitude and distribution of the heat flux, the grid

spacing and the eddy viscosity model. In the following discussion, the sensitivity of the results to these differences is examined in attempt to see which of them, if any, can account for the discrepancies between the current study and JM.

The JM simulations had a constant buoyancy flux of $B_o=1.0$ over the entire source while the present simulation required a buoyancy flux which was tapered as shown in figure 1. This variable buoyancy flux is computed in equation 18 and is characterized by an average value, B_{oavg} , computed by integrating B_o , over the source. With $B_{omax}=1.0$ and $r_{unif}=0.25$, $B_{oavg}=0.42$. To create a more uniform distribution of B_o , r_{unif} was increased to 0.75, which resulted in $B_{oavg}=0.71$. As a final test, the maximum B_o , the value in the r_{unif} region, was modified so that $B_{oavg}=1.0$ and the total buoyancy flux would be the same as JM. Using the constant eddy viscosity model (case T3a), the plume saturated the entire domain well before two rotations, so results for this buoyancy flux are presented with the Smagorinsky model. After two rotations, the horizontally averaged velocity and reduced gravity profiles for these three buoyancy fluxes are compared with the JM simulations as shown in figure~4. An increase in the buoyancy flux does increase the velocity and reduced gravity vertical profiles slightly. The reduced gravity profile exhibits reasonable agreement with JM results, but the velocity is approximately a factor of 2 less than JM for a similar average buoyancy flux. Notice that the plumes grow faster for the constant eddy viscosity cases, which is reasonable because a large thermal diffusivity is present even in the absence of flow. On the other hand, in actual flows, the thermal diffusivity in regions of no flow is very small, as correctly predicted by the Smagorinsky model.

Next, the effect of the eddy viscosity model is examined. As previously discussed, JM use a constant eddy viscosity in both space and time, which is 25 times larger in the horizontal direction than in the vertical direction. In an attempt to obtain a more accurate simulation, the Smagorinsky eddy viscosity model was chosen, which varies in both space and time to represent the changing conditions of the flow, including becoming zero when no flow is present. Three different eddy viscosity models were examined. One with a constant eddy viscosity equivalent to JM and the Smagorinsky model with two different values of the length scale Δ : one which varies in space (equation 16), and one which is constant (equation 17). The resulting horizontally averaged vertical profiles in figure 5 for each of these cases show that the simulation is not particularly sensitive to the eddy viscosity model. Although the shapes of the horizontal velocity and reduced gravity profiles are similar to JM, the velocity magnitudes are smaller by a factor of two.

To check if the finer vertical resolution of the current LES can explain the discrepancy, a simulation with only 23 grid points in the vertical direction is compared with JM, as shown in figure 6. These two Smagorinsky simulations give the same results for both resolutions indicating that the grid size does not account for

the difference between the current LES and JM and that the LES is properly resolved.

Finally, the simulations using the Smagorinsky model at several natural Rossby numbers are shown in figure 7. The current results do show a smaller boundary layer region at the no-slip bottom surface for a smaller Rossby number, which is not reproduced in JM. Even though the velocity profiles are approximately a factor of two less than JM, the shapes of the profiles and the significant decrease in magnitude with the addition of rotation are represented in both simulations.

5.2 Small D/L_x Case

Since the Smagorinsky model tries to reproduce more of the physics of the flow than a constant eddy viscosity model, perhaps a comparison with DNS data will be more favorable. The relevant parameters of both simulations are presented in Table II. The simulation presented in this section is similar to those of the previous section, except that the D/L_x parameter is significantly smaller to match the geometry of the DNS. As a result, changes in the flow due to the differences in the geometry will also be discussed.

This simulation ran for $3\frac{1}{2}$ rotations. After $1\frac{1}{2}$ rotations, rotational effects had not yet become dominant, but, after $3\frac{1}{2}$ rotations, the LES results look more promising. The vertical temperature contours in figure 8 show that the plume has started spreading along the bottom. However, the contours are still symmetric, which are not properly representative of a turbulent flow. On the other hand, the plume in the DNS computation reached the bottom within $1\frac{1}{2}$ rotations as shown in figure 10. The horizontal flow field after $3\frac{1}{2}$ rotations in figure 9 is more similar to the DNS at 1.3 rotations than at 3.3 rotations [20]. Like the DNS, the LES shows vortices that separate from the region under the source and move outward. The horizontal flow fields illustrate the major differences in the flow as a result of changing D/L_x . According to these simulations, the larger D/L_x of 0.5 contains a series of smaller vortices which stay underneath the source while the smaller D/L_x of 0.2 seems to have larger vortices which eventually split from the source and move outward. $D/L_x = 0.4$ in both the experiments of Coates *et al.* [21] and the simulations of Cui and Street [14] is between the two values examined in the current simulations. Their results showed vortices underneath the source with a well defined rim current at the edge of the source. However, they did not mention any observations of vortices propagating away from the source, and JM did not observe a well defined rim current. It is possible that these differences in flow structure beneath the source depends on D/L_x . Brickman and Kelly [9] observed these differences in flow structure in their observations of the evolution of a rotating convective plume. First a tendrill phase, which is convectively dominated, characterized by small, thin plumes.

Second, they call the formation of the horizontal vortices the convecting vortex phase, similar to the horizontal vortex structure of the large D/L_x . Finally, the frontal instability phase occurs when larger scale frontal vortices form, similar to the small D/L_x case. Brickman and Kelly [9] perform experiments with one large D/L_x and one small D/L_x . Though any difference resulting from the different source sizes are not mentioned, pictures of the frontal instability phase are shown only for the small D/L_x case.

Azimuthally averaged quantities for this flow also contain some favorable comparisons with the DNS. The reduced gravity, defined as

$$g' = g \frac{\rho'}{\rho_o} \quad (20)$$

is nondimensionalized by the buoyancy flux as follows:

$$\frac{g'}{(B_o H)^{2/3} / H} = \frac{T}{B_o H / \alpha g \kappa} Ra_f^{1/3} Pr^{1/3} \quad (21)$$

Figure 10 shows that the plume in the LES has not developed as much as in the DNS shown in figure 11, but the plume in the LES has started spreading along the bottom, and the contours have the same general shape and magnitude as the DNS. The azimuthally averaged radial velocity is scaled relative to the buoyancy flux

$$\frac{u_r}{(B_o H)^{1/3}} = \frac{u_r}{\kappa / H} Ra_f^{-1/3} Pr^{1/3} \quad (22)$$

u_r qualitatively resembles the DNS results at time=3.3 Θ but the magnitude is slightly larger. The LES results are more similar to the DNS at time=1.3 Θ . These results emphasize that the development of the flow lags behind the DNS results. The delayed development may be a result of the different top boundary conditions (stress free, distributed source for LES and no-slip, concentrated source for DNS) as well as limitations of the Smagorinsky model in a transitional flow.

6. Summary and Future Work

Though the LES results are qualitatively similar to the DNS, better quantitative agreement is desirable. The Smagorinsky model is unlikely to provide better agreement because of inherent shortcomings of the model, which include inability to correctly predict transitional flows and incorrect behavior in a noninertial reference frame. In addition, in flows with a mean shear, the Smagorinsky model requires a wall function in order to predict correct near wall behavior. However, in the current study, no mean shear is present, so no wall function exists to impose the correct behavior near the solid boundary. In addition, the flow stayed very symmetric for duration of the simulation which is not a physically correct result. However, according to Denbo and Skyllingstad [20], the presence of the horizontal component

of the rotation vector, which was neglected in this study, increases the asymmetry of the flow. Though these results do not agree with the DNS well enough to confidently apply this subgrid scale model to higher speed flows, they do give evidence that a proper subgrid scale model could give very reasonable results for high Rayleigh number flows.

An alternate subgrid scale model which does not have these shortcomings would likely produce more accurate results. For instance, the subgrid scale estimation model has been used successfully in both high Reynolds number flows [22], turbulent convection [23], and rotating turbulent convection [24] and does not require a wall function for correct near wall behavior in shear flows. In addition, the estimation subgrid scale model obeys transformation rules required for the subgrid scale stress tensor in a noninertial frame of reference, and the LES results agree well with DNS data for simple rotating turbulent flows [25,26]. Current work on this project involves applying the estimation subgrid scale model to rotating turbulent convection. Eventually, these methods should enable simulations of higher Rayleigh numbers. As shown in Table III, the maximum Rayleigh number for numerical simulations is still far from that of a realistic geophysical flow.

In spite of inadequacies of the Smagorinsky model in transitional flows, the LES simulations were able to reproduce some of the qualitative features of the flow. The development of the convective plume is similar to the DNS and experimental studies but much slower, which is probably due to a combination of the use of the distributed source boundary condition and the subgrid scale model. The computed velocities are closer to the DNS results than the velocities computed by JM for this case; in this instance, the Smagorinsky model is more accurate than the constant eddy viscosity model.

The present simulations show that the horizontal vortical structure depends on the ratio of the source diameter to domain size (D/L_x). With a small D/L_x , vortices form under the source and propagate away; a larger D/L_x causes small (relative to the source diameter) vortices to remain under the source. These observations are consistent with other studies which also show the development of a rim current at intermediate aspect ratios.

Table I Parameters for LES simulations for $Ro^*=0.1$, $L_x=16$ and source radius=4. Note that the value of Δ is only relevant if the Smagorinsky model is being used.

	Ra_f	Ta	Ro^*	B_{oavg}	ν_T model	Δ	grid
T1	5×10^{10}	3×10^8	0.1	0.42	Smagorinsky	Δ_x	128x128x33
T2	5×10^{10}	3×10^8	0.1	0.42	Smagorinsky	$(\Delta_x \Delta_y \Delta_z)^{1/3}$	128x128x33
T3	5×10^{10}	3×10^8	0.1	0.71	$\nu_T = 25$		128x128x33
T3a	5×10^{10}	3×10^8	0.1	1.00	$\nu_T = 25$		128x128x33
T4	5×10^{10}	3×10^8	0.1	1.00	Smagorinsky	$(\Delta_x \Delta_y \Delta_z)^{1/3}$	128x128x33
T5	5×10^{10}	3×10^8	0.1	1.00	Smagorinsky	$(\Delta_x \Delta_y \Delta_z)^{1/3}$	128x128x23
T6	5×10^{10}	0.0	∞	1.00	Smagorinsky	$(\Delta_x \Delta_y \Delta_z)^{1/3}$	128x128x33
T7	8×10^8	4×10^6	0.33	1.00	Smagorinsky	$(\Delta_x \Delta_y \Delta_z)^{1/3}$	128x128x33
T8	5×10^{10}	3×10^8	0.1	0.42	$\nu_T = 25$		128x128x33
JM1	8×10^8	9.6×10^8	0.1	1.00	$\nu_h = 5; \nu_v = 0.2$		128x128x20
JM2	8×10^8	4×10^6	0.33	1.00	$\nu_h = 5; \nu_v = 0.2$		128x128x20
JM3	8×10^8	400	316	1.00	$\nu_h = 5; \nu_v = 0.2$		128x128x20

Table II Parameters for simulations with $Ro^*=0.1$, $Lx=7.5$, source radius=0.75; LES uses the Smagorinsky model with $\Delta = (\Delta_x \Delta_y \Delta_z)^{(1/3)}$.

	Raf	Ta	Rotation Period $= 4\pi / \sqrt{Ta}$	Grid	Velocity boundary condition	Temperature boundary condition
LES	5×10^{10}	3×10^8	7.25×10^{-4}	128x128x33	Stress free	Insulated
DNS [4]	10^9	2.5×10^7	2.52×10^{-3}	256x256x5	No slip	Dt/dz=-1

Table III Limiting parameters for different methods used for studying rotating convection [10].

Method	Ra_f	Ta
Observations	$>10^{25}$	$>10^{14}$
Experiments	$<10^{20}$	$<10^{10}$
Turbulence simulations	$<10^{10}$	$<10^8$

References

- [1] Gill A.E. Atmosphere-ocean dynamics, Academic Press, New York, 1982.
- [2] Toggweiler J.R., The ocean's overturning circulation, *Phys. Today*, 47 (1994) 45-50.
- [3] Lavelle J.W., Baker E.T., A numerical study of local convection in the benthic ocean induced by episodic hydrothermal discharges, *J. Geophys. Res.*, 99 (1994) 16065-16080.
- [4] Chan D.C., Rotation on turbulent convection generated by an isolated source: A numerical simulation, Ph.D. thesis, University of Southern California, USA, 1996.
- [5] Jones H., Marshall J., Convection with rotation in a neutral ocean: A study of open-ocean deep convection, *J. Phys. Oceanogr.*, 23 (1993) 1009-1039.
- [6] Rossby H.T., A study of Bénard convection with and without rotation, *J. Fluid Mech.*, 36 (1969) 309.
- [7] Boubnov B.M., Golitsyn G.S., Temperature and velocity field regimes of convective motions in a rotating plane fluid layer. *J. Fluid Mech.* 219 (1990) 215-239.
- [8] Fernando H.J.S., Chen R.R., Boyer.D.L., Effects of rotation on convective turbulence, *J. Fluid Mech.*, 228 (1991) 513-547.
- [9] Brickman D., Kelly D.E., Development of convection in a rotating fluid: scales and patterns of motion. *Dyn. Atm. Oceans.* 19 (1993) 389-405.
- [10] Maxworthy T., Narimousa S., Unsteady, Turbulent Convection into a Homogeneous Rotating Fluid, with Oceanographic Applications, *J. Phys. Oceanogr.*, 24 (1994) 865-887.
- [11] Scott J.C., Killworth P.D., Upper ocean structures in the southwestern Iceland Sea – A preliminary report. in: Chu P.C., Gascard J.C. (Eds.), *Deep convection and deep water formation in the oceans*, 1991, pp.87-106.
- [12] Johannessen O.M., Sandven S., Johannessen J.A., Eddy-related winter convection in the Boreas Basin. in: Chu P.C., Gascard J.C. (Eds.), *Deep convection and deep water formation in the oceans*, 1991, pp.87-106.

- [13] Julien K., Legg S., McWilliams J., Werner J., Rapidly rotating turbulent Rayleigh-Bénard convection, *J. Fluid Mech.*, 322 (1996) 243-273.
- [14] Cui A., Street R.L., Large eddy simulation of turbulent rotating convective flow development, *J. Fluid Mech.*, 447 (2001) 53-84.
- [15] Mason P.J., Large-eddy simulation of the convective atmospheric boundary layer, *J. Atmos. Sci.*, 46 (1994) 1492-1516.
- [16] Deardorff J.W. On the magnitude of the subgrid scale eddy coefficient, *J. Comp. Phys.*, 7 (1971) 120-133.
- [17] Lilly D.K. On the application of the eddy viscosity concept in the inertial subrange of turbulence, NCAR Manuscript No. 123, National Center for Atmospheric Research, Boulder Colorado, 1966.
- [18] Eidson T.M., Numerical simulation of the turbulent Rayleigh-Bénard problem, *J. Fluid Mech.*, 158 (1985) 245-268.
- [19] Kimmel S.J., Large eddy simulation of turbulent convection, Ph.D. thesis, University of Southern California, USA, 1998.
- [20] Denbo D.W., Skillingstad E.D., An ocean large-eddy simulation model with applications to deep convection in the Greenland Sea, *J. Geophys. Res.-Oceans*, 101 (1996) 1095-1110.
- [21] Coates M.J., Ivey G.N., Taylor R.J., Unsteady turbulent convection into a rotating linearly stratified fluid: Modeling deep ocean convection, *J. Phys. Ocean.*, 25 (1995) 3032-3050.
- [22] Domaradzki J.A., Saiki E.M., A subgrid-scale model based on the estimation of unresolved scales of turbulence, *Phys. Fluids*, 9 (1997) 2148-2164.
- [23] Kimmel S.J., Domaradzki J.A., Large eddy simulations of Rayleigh-Bénard convection using subgrid scale estimation model, *Phys. Fluids*, 12 (2000) 169-184.
- [24] Kimmel S.J., Domaradzki J.A., Large eddy simulation of rotating turbulent convection using the subgrid scale estimation model, in: Liu C., Sakall L., Beutner T., (Eds.), *DNS/LES--Progress and Challenges Proceedings of the Third AFOSR International Conference on Direct Numerical Simulation and Large Eddy Simulation*, Greyden Press, Arlington, Texas, 2001, pp. 351-358.

[25] Horiuti K., Transformation properties of subgrid-scale models in a frame of reference undergoing rotation, *Modern Simulations S.* (2001) 123.

[26] Domaradzki J.A., Loh K.C., Yee, P.P, Large eddy simulations using the subgrid-scale estimation model and truncated Navier-Stokes dynamics, *Theor. Comp. Fluid Dyn.*, 15 (2002) 421-450.

Figure 1: Computational domain and boundary conditions for rotating finite source convection.

Figure 2: Development of thermal plume for run T1 with $Ra_f=5 \times 10^{10}$, $Ta=3 \times 10^8$, $D/L_x=1/2$.

Figure 3: Horizontal velocity field for run T1 with $Ra_f=5 \times 10^{10}$, $Ta=3 \times 10^8$, and $D/L_x=1/2$.

Figure 4: Effect of varying average surface buoyancy flux for (a) u_H and (b) g' . No symbols: Smagorinsky model, runs T2, T3, T4. Symbols: $v_T=\text{constant}$; o: cases T8, T3; +: JM1.

Figure 5: Effect of varying eddy viscosity model for (a) u_H and (b) g' . No symbols: - T1; -- T2; - T8; Symbols: JM1.

Figure 6: Effect of vertical grid spacing for (a) u_H and (b) g' . No symbols: runs T4, T5; Symbols: JM1.

Figure 7: Effect of varying Ro^* for (a) u_H and (b) g' . No symbols: runs T6, T7, T8; Symbols: JM1, JM2, JM3.

Figure 8 Development of thermal plume for LES with $Ra_f=5 \times 10^{10}$, $Ta=3 \times 10^8$ and $D/L_x=1/5$ at time= 3.5Θ .

Figure 9: Horizontal velocity field for LES with $Ra_f=5 \times 10^{10}$, $Ta=3 \times 10^8$ and $D/L_x=1/5$ at time= 3.5Θ .

Figure 10: Thermal plume for DNS with $Ra_f=10^9$, $Ta=2.5 \times 10^7$ and $D/L_x=1/5$ in the $Y=3.75$ plane ([4] figure 3.79).

Figure 11: Horizontal velocity field through the middle of the domain for DNS with $Ra_f=10^9$, $Ta=2.5 \times 10^7$ and $D/L_x=1/5$ at time= $3\frac{1}{2}\Theta$ ([4] figure 3.83b).

Figure 12: Azimuthally averaged quantities for LES with $Ra_f=5 \times 10^{10}$, $Ta=3 \times 10^8$ and $D/L_x=1/5$ at time= 3.5Θ .

Figure 13: Azimuthally averaged quantities for DNS with $Ra_f=10^9$, $Ta=2.5 \times 10^7$ and $D/L_x=1/5$ at time= $3\frac{1}{2}\Theta$ ([4] figure 3.94b).

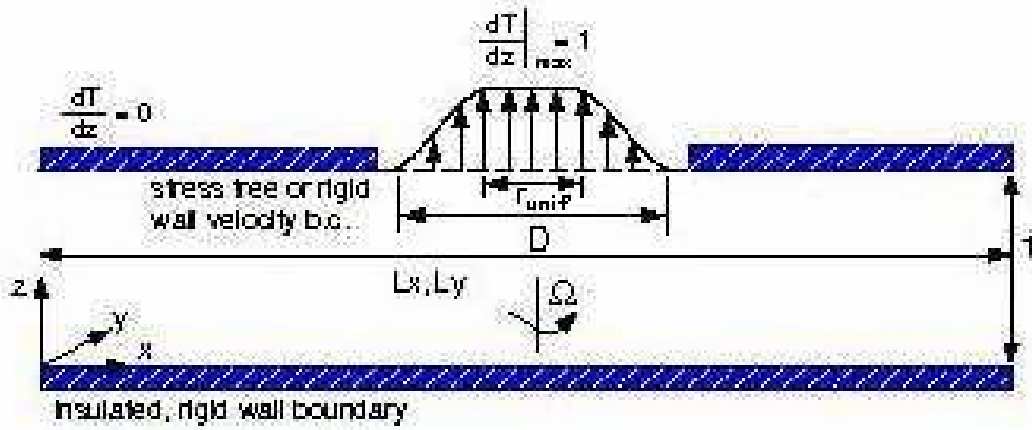


Figure 1

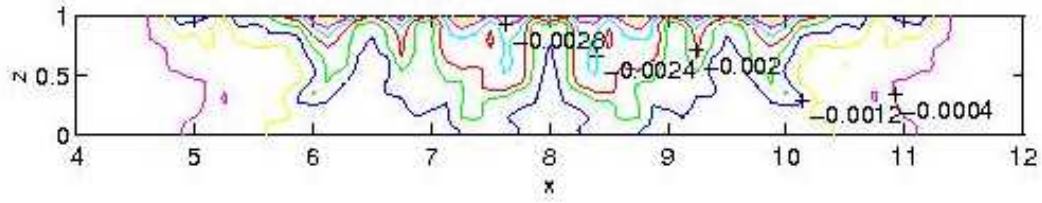
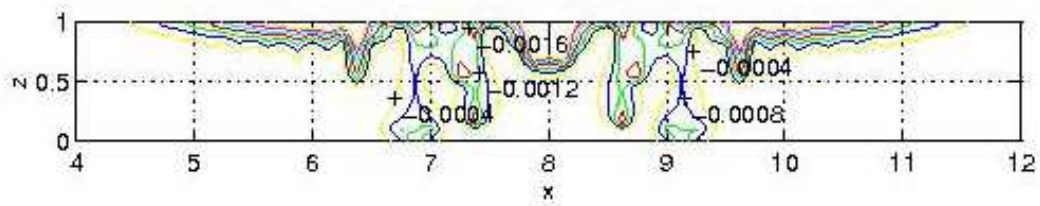
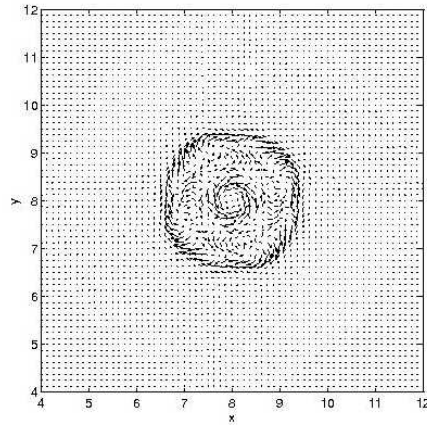
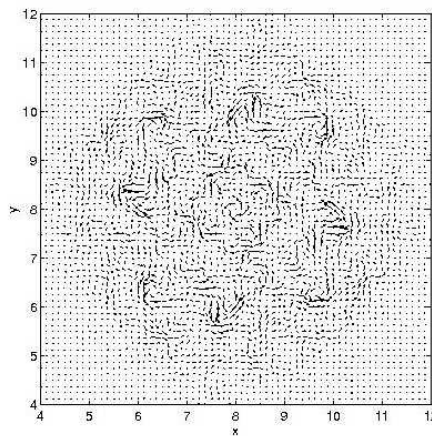
(a) time=1.5 Θ (b) time=3.5 Θ

Figure 2: Development of thermal plume for run T1 with $Ra_f=5 \times 10^{10}$, $Ta=3 \times 10^8$, $D/L_x=1/2$.



(a) time=1.5 Θ ; $z=0.87$



(b) time=3.5 Θ ; $z=0.5$

Figure 3: Horizontal velocity field for run T1 with $Ra_f=5 \times 10^{10}$, $Ta=3 \times 10^8$, and $D/L_x=1/2$.

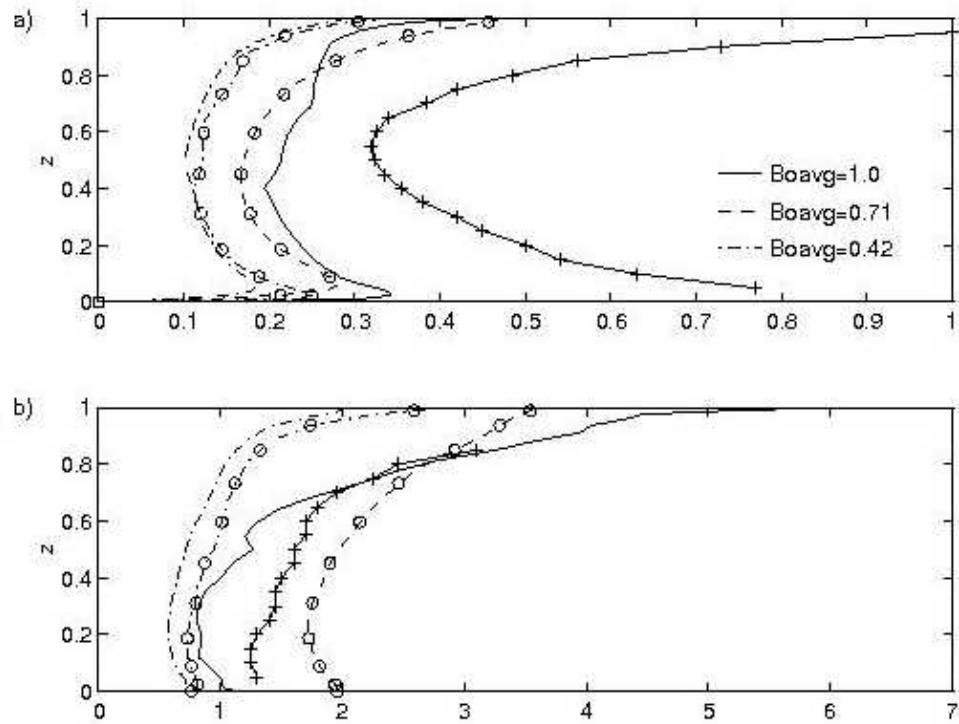


Figure 4: Effect of varying average surface buoyancy flux for (a) u_H and (b) g' . No symbols: Smagorinsky model, runs T2, T3, T4. Symbols: $v_t=\text{constant}$; o: cases T8, T3; +: JM1.

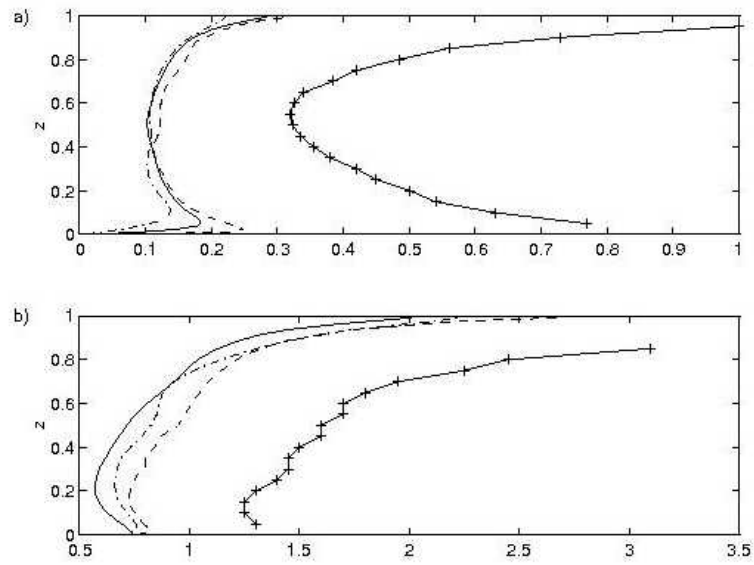


Figure 5: Effect of varying eddy viscosity model for (a) u_H and (b) g' . No symbols: - T1; -- T2; - . T8; Symbols: JM1.

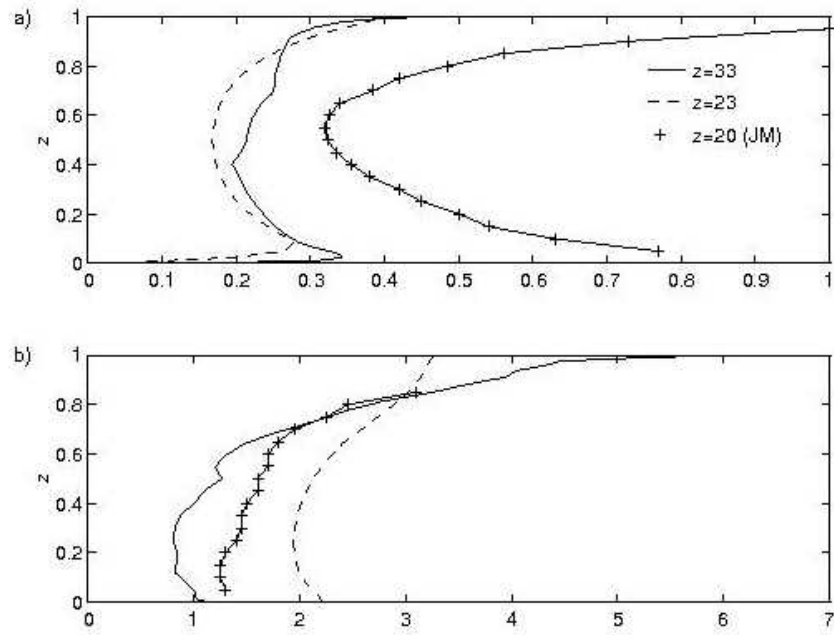


Figure 6: Effect of vertical grid spacing for (a) u_H and (b) g' . No symbols: runs T4, T5; Symbols: JM1.

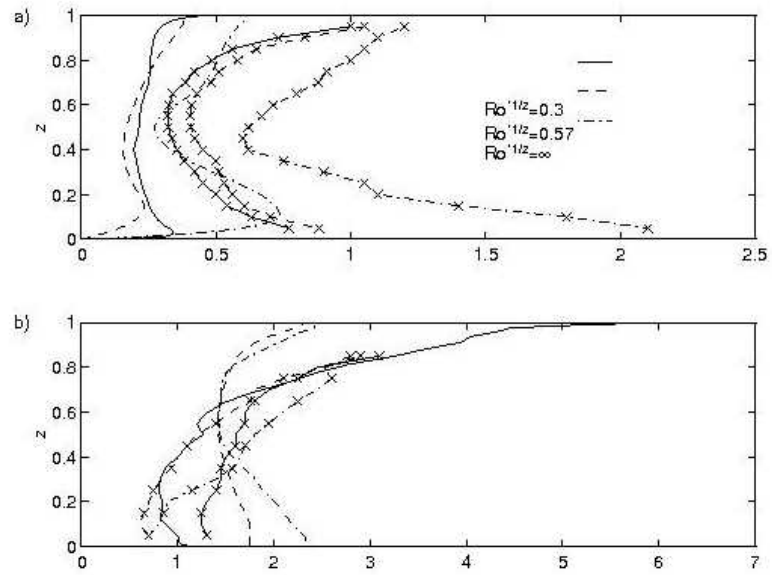


Figure 7: Effect of varying Ro^* for (a) u_H and (b) g' . No symbols: runs T6, T7, T8; Symbols: JM1, JM2, JM3.

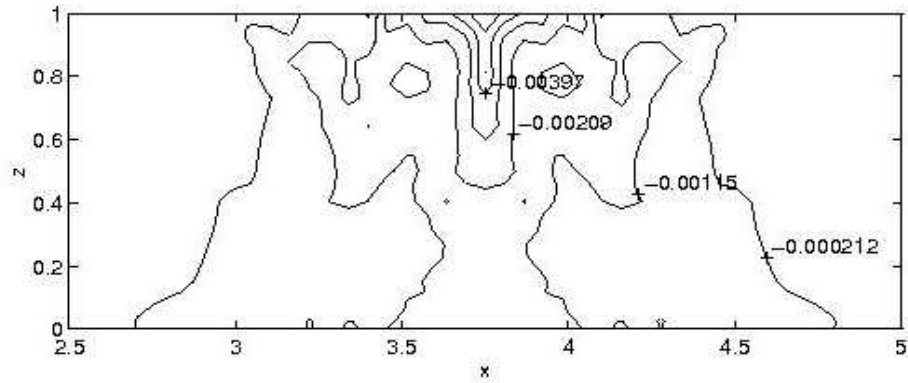


Figure 8 Development of thermal plume for LES with $Ra_f=5 \times 10^{10}$, $Ta=3 \times 10^8$ and $D/L_x=1/5$ at time= 3.5Θ .

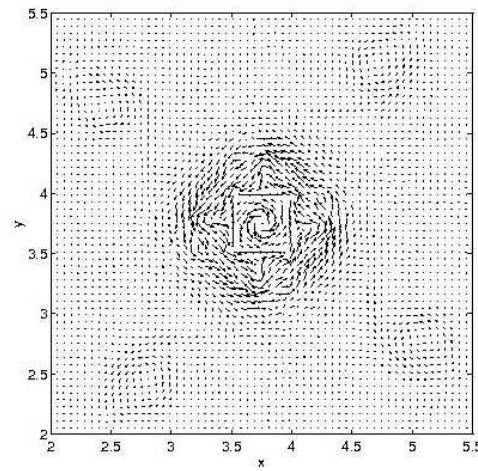


Figure 9: Horizontal velocity field for LES with $Ra_f=5 \times 10^{10}$, $Ta=3 \times 10^8$ and $D/L_x=1/5$ at time= 3.5Θ .

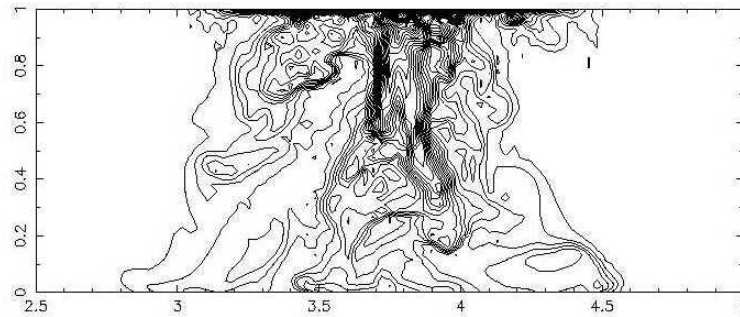
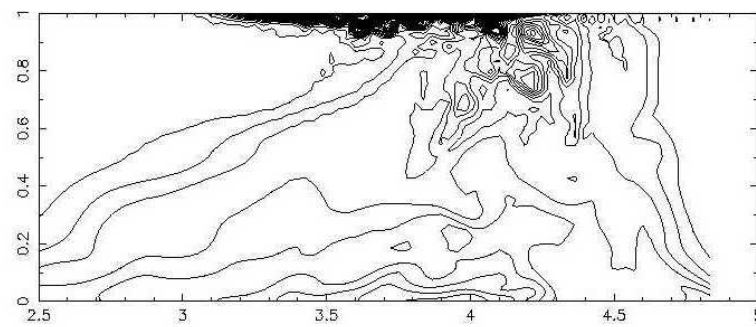
a) time = $1 \frac{1}{2} \Theta$ b) time = $3 \frac{1}{2} \Theta$

Figure 10: Thermal plume for DNS with $Ra_f=10^9$, $Ta=2.5 \times 10^7$ and $D/L_x=1/5$ in the $Y=3.75$ plane. (Chan, 1996, figure 3.79).

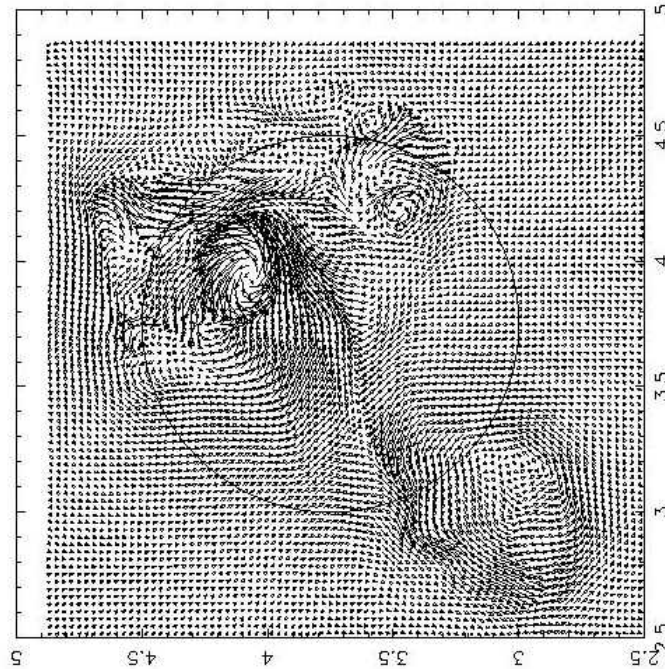
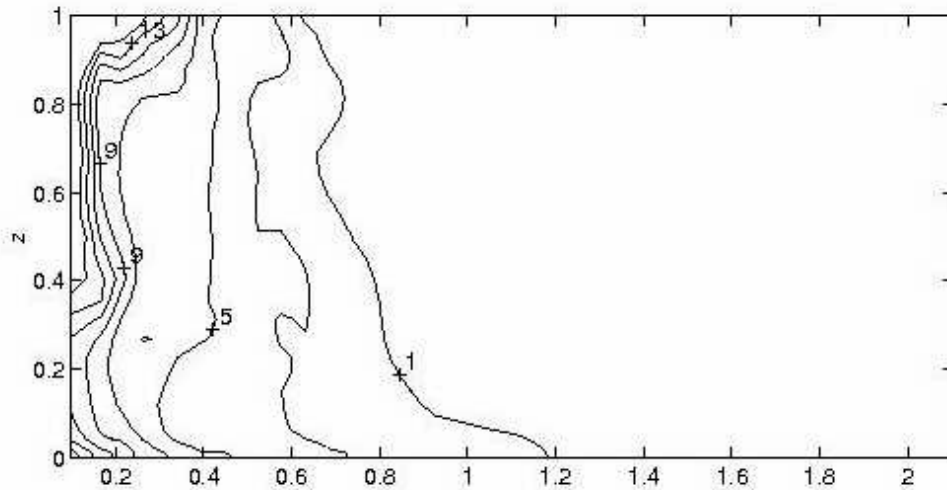
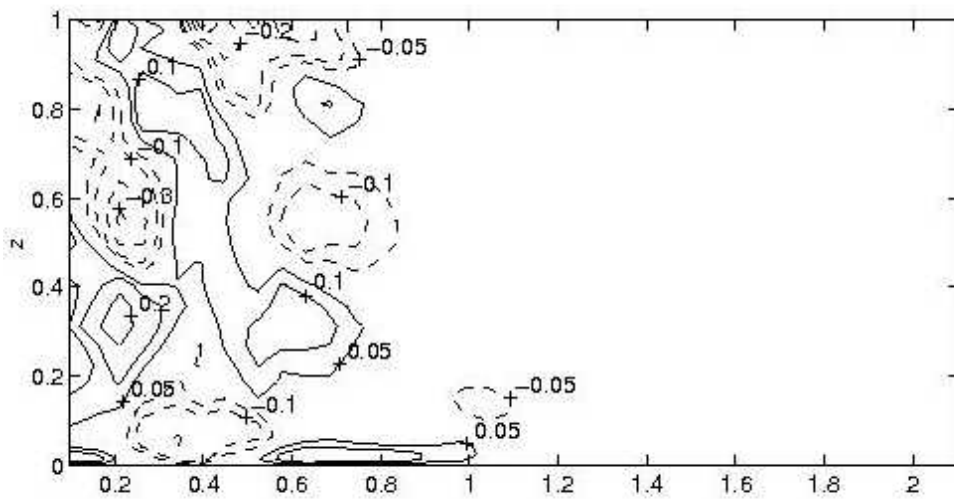


Figure 11: Horizontal velocity field through the middle of the domain for DNS with $Ra_f=10^9$, $Ta=2.5 \times 10^7$ and $D/L_x=1/5$ at time= $3\frac{1}{2}\Theta$. (Chan, 1996, figure 3.83b)

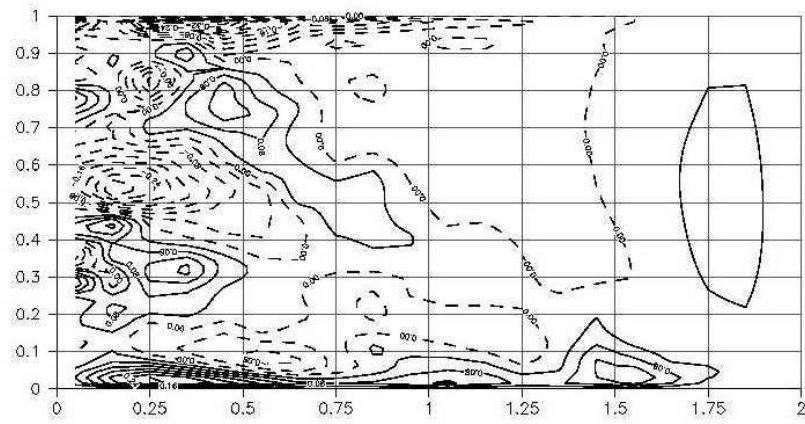


(a) $\frac{g'}{(B_o R)^{2/3} H}$

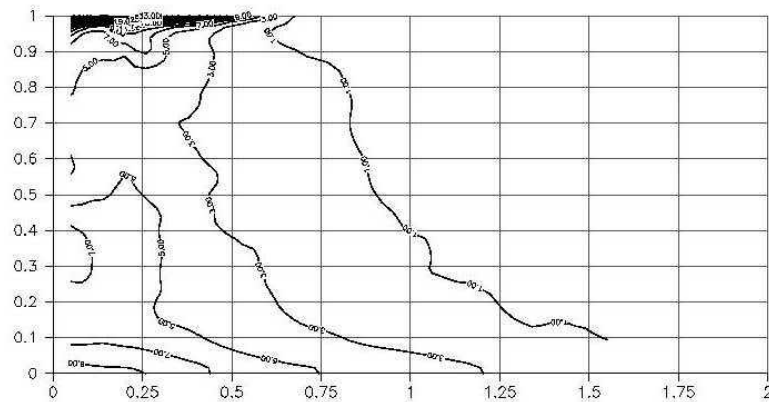


(b) $\frac{u_r}{(B_o R)^{1/3}}$

Figure 12: Azimuthally averaged quantities for LES with $Ra_f=5 \times 10^{10}$, $Ta=3 \times 10^8$ and $D/L_x=1/5$ at time $=3.5\Theta$.



$$(a) \frac{g'}{(B_o R)^{2/3} H}$$



$$(b) \frac{u_r}{(B_o R)^{1/3}}$$

Figure 13: Azimuthally averaged quantities for DNS with $Ra_f=10^9$, $Ta=2.5 \times 10^7$ and $D/L_x=1/5$ at time $=3\frac{1}{2}\Theta$. (Chan, 1996, figure 3.92a; figure 3.94b)